Supporting Information for "What triggers caldera ring-fault subsidence at Ambrym volcano? Insights from the 2015 dike intrusion and eruption"

T. Shreve[1] *, R. Grandin[1], D. Smittarello[2] †, V. Cayol[3], V. Pinel[2], M.

Boichu[4], Y. Morishita[5]

[1]Université de Paris, Institut de physique du globe de Paris, CNRS, F-75005, Paris, France

[2]University Grenoble Alpes, University Savoie Mont Blanc, CNRS, IRD, IFSTTAR, ISTerre, Grenoble, France

[3]Université Clermont Auvergne, CNRS, IRD, OPGC, Laboratoire Magmas et Volcans, F-63000 Clermont-Ferrand, France

[4]Université de Lille, UMR 8518 – LOA – Laboratoire d'Optique Atmosphérique, F-59000, Lille, France

[5]Geospatial Information Authority of Japan, Ibaraki, Japan

File Contents

1. Text S1 to S7

————

*Currently at Earth and Planets

Laboratory, Carnegie Institution for Science,

Washington, District of Columbia, USA

†Currently at the European Center for

Geodynamics and Seismology, 19 rue Josy

Welter, L-7256 Walferdange, Gd Duchy of

Luxembourg

May 14, 2021, 2:05pm

2. Figures S1 to S15

3. Tables S1 to S6

4. Video S1

Introduction

This Supporting Information document includes seven text sections. They discuss in detail:

1. the eruption onset and timing constrained by satellite remote sensing,

2. the processing and uncertainty of the Pléiades digital elevation model (DEM),

3. the mass of co-eruptive gas emission as measured by satellite remote sensing,

4. InSAR data processing,

5. data preparation for the inversion,

6. the 3D Mixed Boundary Element Method, and

7. the appraisal step of the non-linear inversion.

It also includes fifteen supporting figures, which supplement the manuscript's main text and figures, and six tables recording the DEM uncertainties, SAR datasets, post-processing parameters, and final parameter estimates from the inversions. Finally, there is one supporting video, which shows an animation of the deformation sources' 3D geometry, as estimated in Inversion 3.

Text S1: Eruption Onset and Timing

SO_2 lifetime in the atmosphere may exceed the time interval between two consecutive SO_2 satellite acquisitions, equal to 12 or 24 hours with thermal infrared (e.g. IASI) or ultraviolet (e.g. OMPS) sensors, respectively. Hence, SO_2 observations on two consecutive

satellite overpasses may measure twice the same parcel of SO_2. As a consequence, simply assuming daily or bi-daily SO_2 mass burden derived from satellite measurements provides an upper bound for the SO_2 mass released during the eruption. The bounds on the SO_2 mass estimate (shown in light blue in Figure 1e in the main text) are determined by varying the SO_2 column amount detection limit from 2 Dobson Units (DU) to 0.8 DU. Only pixels associated to SO_2 column amounts exceeding these each thresholds are included in the daily mass calculation (see Fig. S2, which also includes a MODVOLC thermal anomaly time series (Wright et al., 2004; Wright, 2016)). On 21 February 2015, the OMPS satellite made acquisitions in Zoom Mode, and the Level 2 middle tropospheric (TRM) data products were not accessible. The SO_2 mass for this day was estimated using NASA's website (`https://so2.gsfc.nasa.gov/pix/daily/ixxxza/loopall_omps.php ?yr=15&mo=02&dy=21&bn=vanuatu`).

To further constrain the eruption onset time, we use the National Oceanic and Atmospheric Administration (NOAA) Air Resources Laboratory's (ARL) Hybrid Single-Particle Lagrangian Integrated Trajectory model (HYSPLIT) (`https://www.ready.noaa .gov/HYSPLIT_traj.php`) to find the back-trajectory of SO_2 parcels in the leading edge of the eruption's volcanic plume (Stein et al., 2015; Crawford et al., 2016). The initialization parameters were set to an altitude of 8 km at the plume's leading edge, as measured using SO_2 height retrieval algorithms developed for observations from the Infrared Atmospheric Sounding Interferometer (IASI) (Clarisse et al., 2014). The forefront of the plume was located, and correspondingly initialized, near 159.1°E, 17.53°S at 10:30 AM UTC 21 February (see Figure S2b). Using the Global Data Assimilation System (GDAS) 1° global meteorological model, HYSPLIT estimates that the SO_2 parcels were injected into the

atmosphere from Ambrym between 15:00 and 16:00 UTC 20 February at an altitude of $\sim$8800 m above ground level, consistent with the time-frame established by MIROVA for the onset of the eruption.

At the end of the eruption, MODVOLC, a volcanic thermal alert detection system (see Figure S2d), did not detect any thermal anomalies between 22 and 28 February. On the other hand, during the same time interval using MIROVA, two thermal anomalies were still present in Marum, with no thermal anomalies present in Benbow (Coppola, Laiolo, & Cigolini, 2016). Although both MODVOLC and MIROVA detection algorithms use observations from the moderate resolution imaging spectro-radiometer (MODIS) sensors mounted on NASA's satellite Terra and Aqua (Figure S2c), MODVOLC detects and classifies thermal anomalies based on a normalized difference between radiance in the long-wave infrared (LWIR, 12.02 μm) and middle infrared (MIR, 3.959 μm) spectrums, and a pixel is considered a thermal anomaly if this normalized difference is greater than an empirically-established threshold (Wright et al., 2004; Wright, 2016). MIROVA, on the other hand, uses a normalized and enhanced thermal index, as well as including a spatial analysis, resulting in more sensibility to local hotspot detection, explaining the discrepancy between these two systems (Coppola, Laiolo, Cigolini, Delle Donne, & Ripepe, 2016).

Text S2: Lava Flow Digital Elevation Model

We used MicMac software and Pléiades satellite imagery to construct a Digital Elevation Model (DEM) of the lava flow (Rupnik et al., 2018)(`http://logiciels.ign.fr/ ?Micmac`). We calculated the DEM from two 50 cm Pléiades panchromatic images acquired after the eruption (one on 20 March 2015 at 23:15 UTC and another on 30 September 2017 at 23:00 UTC).

The DEM was downsampled to 12 m, the resolution of the pre-eruption TanDEM-X (TDX) DEM. Due to the spatial extent of the lava flow (>2.5 km^2), a coarser resolution should not bias the lava flow volume calculation. We then subtracted this downsampled DEM from the TDX DEM. There was an elevation ramp visible across this DEM difference, which could possibly be due to the lack of absolute calibration of the Pléiades DEM with Ground Control Points, or due to topography-related height errors. We masked the lava flow to obtain a reference region where no topographic change occurred, removed unreasonable values between -15.5 m and 15.5 m, and calculated the mean. We then removed the mean, $\mu = 1.4268$ m, the best-fitting plane, and the unreasonable values from the original Pléiades DEM. The difference between this final Pléiades DEM, and the TDX DEM is shown in Figure S1a. The total volume of the lava flows was estimated to be $\sim12.4\times10^6$ m^3, with an average height of ~5 m.

Uncertainty Estimates

To estimate the uncertainty of the lava flow volume, we follow the method of Bagnardi, González, and Hooper (2016) and Favalli et al. (2010). These estimates calculate uncertainties associated with both spatially correlated and uncorrelated errors. We fit σ and λ of an exponential, $C_r = \sigma^2 \exp(\frac{-r}{\lambda})$, where r is the distance between two pixels, to the covariograms of three control areas (see Figure S1 and Table S1). The equation for uncertainties given variance propagation when all errors are spatially correlated is the following

$$\sigma_V^2 = A^2 \sum_i \sum_j C_{ij}, \tag{1}$$

where A is a pixel's surface area and C_{ij} is the covariance between the height error of pixels i and j.

Given the covariances shown in Figure S1b, we note that pixels separated by less than

∼60 m are spatially correlated for all control areas (pixel size of 12.1 × 12.1 m). We can

therefore simplify Equation 1 to

$$\sigma_V^2 = A^2 N(\sigma_Z^2 + \sum_{r=1}^{n} C_r),$$ (2)

where σ_Z is the uncorrelated elevation standard deviation in each control area (see Table

S1), N is the number of pixels, and $n = 5$ when pixels are correlated within ∼60 m. Given

the estimates of σ and λ for the three control areas, the σ_V estimates for $N = 18721$ (the

size of the lava flow) are 0.048, 0.041, and 0.035 ×10^6 m^3. The average σ_V is 0.041 × 10^6

m^3. We conclude that the lava flow volume estimate, including an error of two standard

deviations from the mean, is 12.4 (±0.08) ×10^6 m^3. If we assume an average vesiculation

of basaltic a'a lava flows to be 25%, similar to Bagnardi et al. (2016), we obtain an

adjusted volume of 9.3 (±0.08) ×10^6 m^3 DRE.

Even within the caldera, which is relatively flat, we still observe elevation errors that

correlate with topographic relief and errors due to the presence of vegetation. A tri-stereo

Pléiades acquisition would decrease the uncertainty due to topography. Nonetheless, the

error on the total volume is less than 2%.

Text S3: SO$_2$ Mass Calculation

Near the eruptive vent, IASI measured a volcanic plume altitude of ∼5 km on 21

February ∼10:30 UTC. HYSPLIT trajectories showed that, if parcels were initiated at 5

km altitude at 3h00 21 February (approximate time of UV spectrometer Ozone Mapping

and Profiler Suite (OMPS) Zoom acquisition (Li et al., 2017)), they would travel first

to the west, then circulate counter-clockwise back eastwards towards Ambrym, finally

travelling to the southeast on 24 February (see Fig. S2a). The parcels' altitudes would

range betweeen 5–7 km. We assumed that any SO_2 measured after the end of the eruption was due to the recirculation of SO_2 parcels in the region. The SO_2 mass is overestimated, as the same SO_2 parcels were likely measured on two consecutive dates. We resampled the OMPS products using Delaunay triangulation to a regular grid, and applied a threshold of between 0.8–2 Dobson Units (DU, where 1 DU $= 2.69 \times 10^{16}$ molecules/cm^2) before calculating the total SO_2 mass.

As mentioned in the main text, we conservatively estimated ∼40 kt of SO_2 emitted during the eruption. Given the small crystal fraction (<5 wt%) of eruptive products at Ambrym (Allard et al., 2015), we can use the relationship

$$V_l = \frac{T_{SO_2} w_{S,gas}}{\rho_m w_{S,\,melt}} \tag{3}$$

to calculate the total volume of degassed lava V_l, where T_{SO_2} is the total mass of emitted SO_2, $w_{S,gas} = 50$ wt% is the weight percent of sulphur in SO_2, $w_{S,\,melt} = 0.075$ wt% is the weight percent of sulphur in the melt, and $\rho_m \approx 2800$ kg m^{-3} is the magma density. This corresponds to 9.5×10^6 m^3 of degassed lava, consistent with the erupted volume.

Text S4: Geodetic Data Processing

Ascending Stripmap-to-Stripmap Interferograms

The coregistration, topographic and orbital fringe removal, interferogram formation, multilooking, and geocoding steps are performed using the Interferometric SAR scientific computing environment (ISCE)(Rosen et al., 2012), while filtering and unwrapping are performed with NSBAS modules (Doin et al., 2011). Topographic fringes are removed with DLR's TanDEM-X 12 meter global DEM (an average of DEM's acquired before November 2014) (Wessel, 2016).

The phase is most coherent in regions with little vegetation, such as in the western portion of Ambrym's caldera. The interferogram near-field (areas which show more than 1 m of surface displacement, SW of the eruptive fissure) is multilooked 2 times in range and 4 times in azimuth, while the far-field is multilooked 8 times in range and 16 times in azimuth. Higher multilooking in the densely vegetated far-field increases coherence, while preserving the broad, long-wavelength signature of the signal.

Filtering and Unwrapping

The filtering and unwrapping procedure is the same for both the ascending and descending interferograms. The interferometric phase is smoothed using a weighted power spectrum filter (Rosen et al., 2004), followed by a cascading high-pass filter (Grandin et al., 2012). Due to the high gradient of interferometric fringes near the fissure, we unwrap the interferograms using an iterative, coherence-based method called MPD, which is a module in NSBAS (Grandin et al., 2012). This method uses the interferogram's coherence to optimize the unwrapping path. Unwrapping begins at a chosen seed pixel that is above a certain coherence threshold. At each iteration, MPD slightly decreases the coherence threshold, and unwraps the nearby pixels above the new threshold. Pixels below the minimum coherence threshold, γ_{min}, will not be unwrapped. For the ascending interferogram, the seed pixel is located southwest of the main fissure in the near-field interferogram and northwest of Benbow in the far-field interferogram. For both the near- and far-fields of the ascending interferogram, $\gamma_{min,asc} = 0.05$, given a maximum coherence of 1.0. For the descending interferogram, $\gamma_{min,desc} = 0.1$.

MPD is advantageous because the iteration number depends on the pixel coherence, and can be used to mask the final, unwrapped interferogram, acting as a proxy for con-

fidence in the unwrapped phase value. For the ascending interferogram, we mask the near-field and the far-field with a threshold of 25000 and 15000 iterations, respectively. The descending interferogram is masked at 14000 unwrapping iterations. These filtered, unwrapped interferograms are then geocoded with ISCE. The far-field of the ascending interferogram is then oversampled to the near-field resolution, resulting in a pixel posting of ~14 m×14 m after geocoding. The descending interferogram has a pixel posting of ~30 m×20 m after geocoding. Finally, we mask the 2015 lava flow, as well as incoherent regions near the fissure and caldera rim. We also apply a water mask to the island.

Bridges connect fringes that are determined, by eye, to be continuous, but which pass through incoherent regions. Without bridges, MPD would not unwrap correctly across the incoherent regions, resulting in unwrapping errors. Remaining unwrapping errors are masked by hand. Interferograms are then referenced to the median of a box to the northwest of the caldera, near 168.07°E, 16.23°S. Due to more than 1 m of line of sight (LOS) motion, the phase contribution from atmospheric effects (which can be more than 10 cm in tropical regions) was negligible, and no atmospheric corrections were applied.

Text S5: Data Subsampling

The data are subsampled using an adaptive quadtree decomposition algorithm, which finely samples areas characterised by mean displacements or displacement gradients above empirically-derived thresholds (Table S4 and Fig. S5) (Walstead, 1999; Jónsson et al., 2002). The algorithm first divides the image into four equal-sized blocks, and within each block, the average deformation value, $\overline{d}$, and the deformation gradient, $\Delta d = d_{max} - d_{min}$, are calculated. Each block is further divided into four equal-sized blocks if either Δd or $\overline{d}$ are above a given threshold, until the block size reaches a minimum size. The displacement

:

value at the center of each block is then used as an input for the non-linear inversion. Respectively, 1329 and 1229 data points are included in the inversion for the ascending and descending interferograms (Fig. S5).

Text S6: Displacement Discontinuity and Direct Boundary Element Methods

The displacement discontinuity method approximates a boundary as N elements, and solves the system of equations $\boldsymbol{AB} = \boldsymbol{P}$, where $\boldsymbol{P}$ is the vector of $3N$ imposed traction conditions, $\boldsymbol{A}$ is the matrix of influence coefficients which relates a unit displacement across element j to the stress on the centroid of element i according to linear elasticity. Finally, $\boldsymbol{B}$ is the vector of $3N$ amplitudes of displacements D_j across an element ($D_j = u_j^+ - u_j^-, j = (x, y, z)$, where u_j^+ and u_j^- are the displacement on the positive and negative sides of j). $\boldsymbol{B}$ is the only unknown, and can be found by solving the system of $3N$ linear equations with $3N$ unknowns. After inverting for D_j, stresses and displacements anywhere within the finite elastic body can be calculated using the sum of known analytical solutions of displacement across a planar element (Crouch, 1976).

The direct method, on the other hand, solves for unknown displacements and stresses on the boundary, as opposed to first solving for the amplitude of displacements (Lachat & Watson, 1976). This is done by leveraging the reciprocal theorem (Sokolnikoff, 1956), considering reciprocity of work between the unknown boundary conditions of the current problem and the boundary conditions of a problem with a known analytical solution. In this case, the latter is a point load in an infinite body. We can then set up and solve a system of equations $\boldsymbol{HU} = \boldsymbol{F}$. $\boldsymbol{H}$ is the matrix of influence coefficients computed by evaluating the boundary integral of stresses produced on element j by a unit load on element i in an infinite medium, and the integrals of displacements produced on element j by a

unit load on element i. $\boldsymbol{F}$ is a known vector of size $3N$, including the prescribed boundary tractions, and $\boldsymbol{U}$ is the vector of $3N$ unknowns corresponding to the displacement on the boundary Γ of a finite elastic body Ω (Cayol & Cornet, 1997). Between these two methods, the former is numerically stable for fractures, while the latter is more exact and computationally efficient for massive boundaries (such as topographies and pressurized magmatic reservoirs).

Text S7: Neighborhood Algorithm Appraisal

The appraisal problem is essentially an interpolation of the multidimensional parameter space, constructing an approximate PPD using 10000 resampled points through a random walk (Gibb's sampling) of the Voronoi cells of the forward models calculated in Section 4.3 of the main text (Sambridge, 1999). No further forward models need to be calculated, as the PPD of each Voronoi cell is considered uniform. The only calculations, for each step, include that of the intersection between Voronoi cells along each axis i in the parameter space, as well as the direction in which the next step will occur. This will always be in the direction of higher probability density (lower misfit).

Video S1: 3D Animation

The file Video_S1.mp4 includes an animation of the 3D geometry of the dike intrusion, deflating reservoir, and caldera ring-fault. The sources in this video were estimated in Inversion 3.

References

Allard, P., Aiuppa, A., Bani, P., Métrich, N., Bertagnini, A., Gauthier, P., ... Garaebiti, E. (2015). Prodigious emission rates and magma degassing budget ofmajor, trace and radioactive volatile species from Ambrym basaltic volcano, Vanuatu island Arc.

Journal ofVolcanology and Geothermal Research, *304*, 378 – 402. doi: 10.1016/
j.jvolgeores.2015.08.022

Bagnardi, M., González, P. J., & Hooper, A. (2016). High-resolution digital elevation
model from tri-stereo Pleiades-1 satellite imagery for lava flow volume estimates
at Fogo Volcano. *Geophysical Research Letters*, *43*(12), 6267–6275. doi: 10.1002/
2016GL069457

Cayol, V., & Cornet, F. H. (1997). 3D mixed boundary elements for elastostatic defor-
mation field analysis. *International journal of rock mechanics and mining*, *34*(2),
275–287. doi: 10.1016/S0148-9062(96)00035-6

Clarisse, L., Coheur, P. F., Theys, N., Hurtmans, D., & Clerbaux, C. (2014). The 2011
Nabro eruption, a SO_2 plume height analysis using IASI measurements. *Atmospheric
Chemistry and Physics*, *14*(6), 3095–3111. doi: 10.5194/acp-14-3095-2014

Coppola, D., Laiolo, M., & Cigolini, C. (2016). Fifteen years of thermal activity at
Vanuatu's volcanoes (2000 - 2015) revealed by MIROVA. *Journal of Volcanology and
Geothermal Research*, *322*, 6–19. doi: 10.1016/j.jvolgeores.2015.11.005

Coppola, D., Laiolo, M., Cigolini, C., Delle Donne, D., & Ripepe, M. (2016). Enhanced
volcanic hot-spot detection using MODIS IR data: Results from the MIROVA sys-
tem. *Geological Society Special Publication*, *426*(1), 181–205. doi: 10.1144/SP426.5

Crawford, A. M., Stunder, B. J., Ngan, F., & Pavolonis, M. J. (2016). Initializing
HYSPLIT with satellite observations of volcanic ash: A case study of the 2008
Kasatochi eruption. *Journal of Geophysical Research*, *121*(18), 10,786–10,803. doi:
10.1002/2016JD024779

Crouch, S. L. (1976). Solution of plane elasticity problems by the displacement disconti-

nuity method. *International Journal for Numerical Methods in Engineering*, *10*(2), 301–343.

Doin, M.-P., Lodge, F., Guillaso, S., Jolivet, R., Lasserre, C., Ducret, G., ... Pinel, V. (2011). Presentation of the small baseline NSBAS processing chain on a case example: the Etna deformation monitoring from 2003 to 2010 using Envisat data. In *Proceedings of the esa 'fringe 2011 workshop', frascati, italy, (19-23 september 2011)* (pp. 19–23).

Favalli, M., Fornaciai, A., Mazzarini, F., Harris, A., Neri, M., Behncke, B., ... Boschi, E. (2010). Evolution of an active lava flow field using a multitemporal LIDAR acquisition. *Journal of Geophysical Research: Solid Earth*, *115*(11), 1–17. doi: 10 .1029/2010JB007463

Grandin, R., Doin, M.-P., Bollinger, L., Pinel-Puysségur, B., Ducret, G., Jolivet, R., & Sapkota, S. N. (2012). Long-term growth of the Himalaya inferred from interseismic InSAR measurement. *Geology*, *40*(12), 1059. doi: 10.1130/G33154.1

Jónsson, S., Zebker, H., Segall, P., & Amelung, F. (2002). Fault slip distribution of the 1999 M$_w$ 7.1 Hector Mine, California, earthquake, estimated from satellite radar and GPS measurements. *Bulletin of the Seismological Society of America*, *92*(4), 1377–1389. doi: 10.1785/0120000922

Lachat, J. C., & Watson, J. O. (1976). Effective numerical treatment of boundary integral equations: A formulation for three-dimensional elastostatics. *International Journal for Numerical Methods in Engineering*, *10*(5), 991–1005. doi: 10.1002/ nme.1620100503

Li, C., Krotkov, N. A., Carn, S., Zhang, Y., Spurr, R. J., & Joiner, J. (2017). New-

generation NASA Aura Ozone Monitoring Instrument (OMI) volcanic SO$_2$ dataset:
Algorithm description, initial results, and continuation with the Suomi-NPP Ozone
Mapping and Profiler Suite (OMPS). *Atmospheric Measurement Techniques*, *10*(2),
445–458. doi: 10.5194/amt-10-445-2017

Rosen, P. A., Gurrola, E., Sacco, G. F., & Zebker, H. (2012, April). The InSAR scientific computing environment. In *Eusar 2012; 9th european conference on synthetic aperture radar* (p. 730-733).

Rosen, P. A., Hensley, S., Peltzer, G., & Simons, M. (2004). Updated Repeat Orbit Interferometry Package Released. *Eos*, *85*(5), 47.

Rupnik, E., Pierrot-Deseilligny, M., & Delorme, A. (2018). 3D reconstruction from multi-view VHR-satellite images in MicMac. *ISPRS Journal of Photogrammetry and Remote Sensing*, *139*, 201–211. doi: 10.1016/j.isprsjprs.2018.03.016

Sambridge, M. (1999). Geophysical inversion with a neighbourhood algorithm— II. Appraising the ensemble. *Geophysical Journal International*, *138*(2), 727–746. doi: 10.1046/j.1365-246X.1999.00876.x

Shreve, T. (2020). *Crustal deformation at Ambrym (Vanuatu) imaged with satellite geodesy: constraints on magma storage, migration, and outgassing* (Unpublished doctoral dissertation). Institut de Physique du Globe de Paris.

Shreve, T., Grandin, R., Boichu, M., Garaebiti, E., Moussallam, Y., Ballu, V., . . . Pelletier, B. (2019). From prodigious volcanic degassing to caldera subsidence and quiescence at Ambrym (Vanuatu): the influence of regional tectonics. *Scientific Reports*, *9*(18868). doi: https://doi.org/10.1038/s41598-019-55141-7

Smittarello, D., Cayol, V., Pinel, V., Peltier, A., Froger, J. L., & Ferrazzini, V. (2019).

Magma Propagation at Piton de la Fournaise From Joint Inversion of InSAR and GNSS. *Journal of Geophysical Research: Solid Earth*, *124*(2), 1361–1387. doi: 10 .1029/2018JB016856

Sokolnikoff, I. (1956). *Mathematical theory of elasticity.* New York: McGraw-Hill.

Stein, A. F., Draxler, R. R., Rolph, G. D., Stunder, B. J., Cohen, M. D., & Ngan, F. (2015). NOAA's hysplit atmospheric transport and dispersion modeling system. *Bulletin of the American Meteorological Society*, *96*(12), 2059–2077. doi: 10.1175/ BAMS-D-14-00110.1

Walstead, S. T. (1999). *Fractal and wavelet image compression techniques.* Bellingham, Washington: SPIE Optical Engineering Press.

Wessel, B. (2016). *TanDEM-X Ground Segment - DEM Products Specification Document* (Tech. Rep. No. 3.1). Oberpfaffenhofen, Germany: EOC, DLR. Retrieved from `https://tandemx-science.dlr.de/` doi: DOI:10.1002/hyp.3360050103

Wright, R. (2016). MODVOLC: 14 years of autonomous observations of effusive volcanism from space. *Geological Society, London, Special Publications*, *426*, 23–53. doi: 10 .1144/SP426.12

Wright, R., Flynn, L. P., Garbeil, H., Harris, A. J. L., & Pilger, E. (2004). MODVOLC: Near-real-time thermal monitoring of global volcanism. *Journal of Volcanology and Geothermal Research*, *135*(1-2), 29–49. doi: 10.1016/j.jvolgeores.2003.12.008
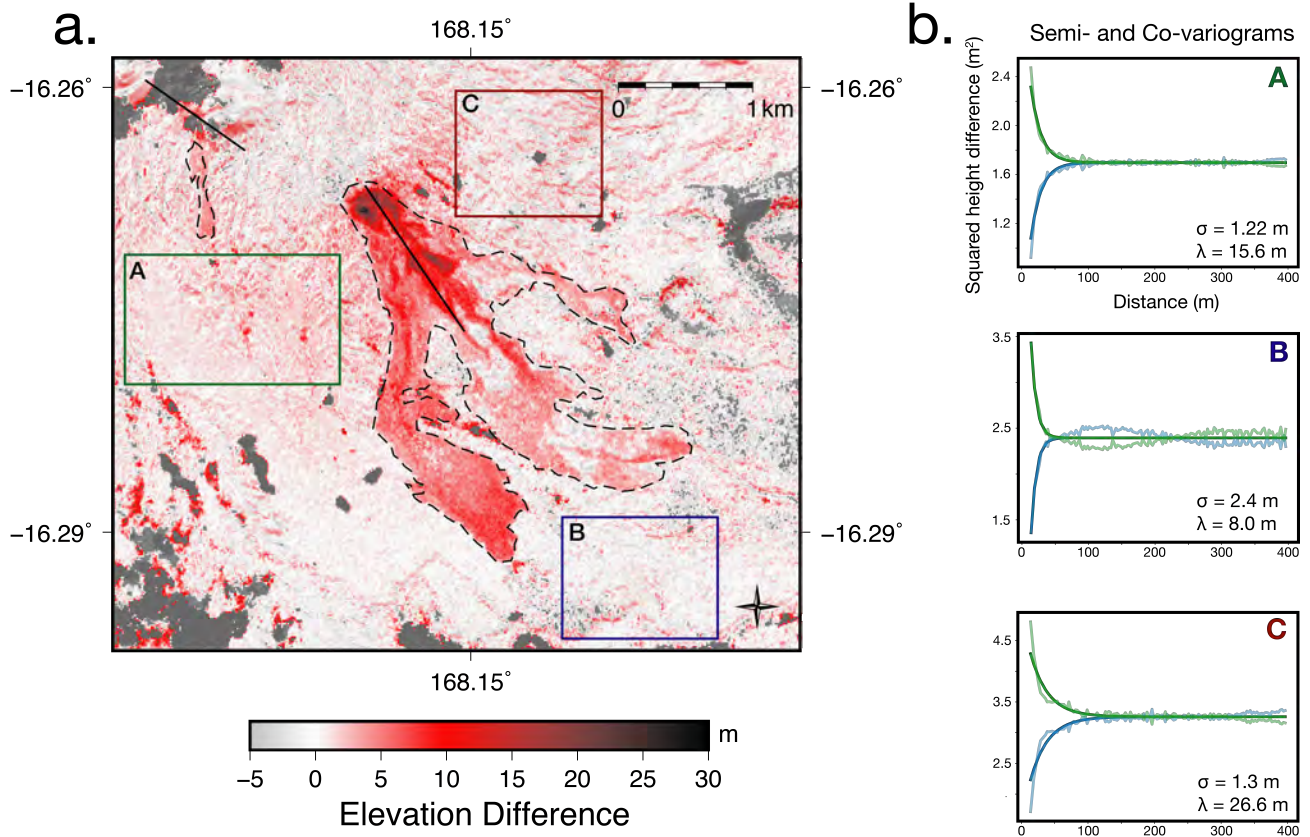
Figure S1. **a.** The elevation difference between DEM's pre- and post- February 2015, as explained in Text S2. The main and secondary flows are outlined with dotted lines, new fissures are mapped with solid lines, and the control areas are outlined with solid, colored lines. Adapted from Shreve et al. (2019). **b.** The semi- and co-variograms for each of the control areas (light colored lines), and the best-fitting exponentials (solid colored lines). The estimates for σ and λ are shown.

Table S1. DEM statistical analysis of three control areas, including the surface area, mean

elevation, and spatially uncorrelated elevation standard deviation.

Control area	Surface area ($\times 10^6$ m^2)	Mean elevation, μ_Z (m)	Uncorrelated elevation standard deviation, σ_Z (m)
A	1.62	1.11	1.40
B	1.10	-0.299	1.64
C	1.06	0.233	1.87

Table S2. SAR datasets used in this study.

Primary acquisition date (UTC)	Secondary acquisition date (UTC)	Sensor	Mode	Geometry/Track	Heading/Look Angle	Data type
2015/01/24 13:14	2015/03/21 13:14	ALOS-2	Stripmap (SM3)	Ascending T101	-13.6°/39.7°	InSAR/azimuth pixel offsets
2015/01/24 13:14	2015/04/04 13:14	ALOS-2	Stripmap (SM3)	Ascending T101	-13.6°/39.7°	MAI
2015/1/17 00:24	2015/03/14 00:24	ALOS-2	Wideswath (WD1)/ Stripmap (SM3)	Descending T203	192.7°/33°	InSAR
2015/02/13 06:13	2015/02/25 06:13	CSK	Stripmap (H4-04)	Descending	192.8°/32.2°	Range/azimuth pixel offsets

Table S3. Specifications for pixel offset post-processing, including mask-

ing and filtering.

Measurements	Displacement bounds	Filter	SNR Mask
ALOS-2 azimuth pixel offsets	-2.7 m$< \Delta x < 1.6$ m	None	$\Delta x_{SNR} < 8$
CSK range pixel offsets	-1.5 m$< \Delta x < 3$ m	None	$\Delta x_{SNR} < 5$
CSK azimuth pixel offsets	-2.7 m$< \Delta x < 1.6$ m	Median filter, block size 500 m $\times$ 500 m	$\Delta x_{SNR} < 5$

Table S4. Quadtree specifications for downsampling.

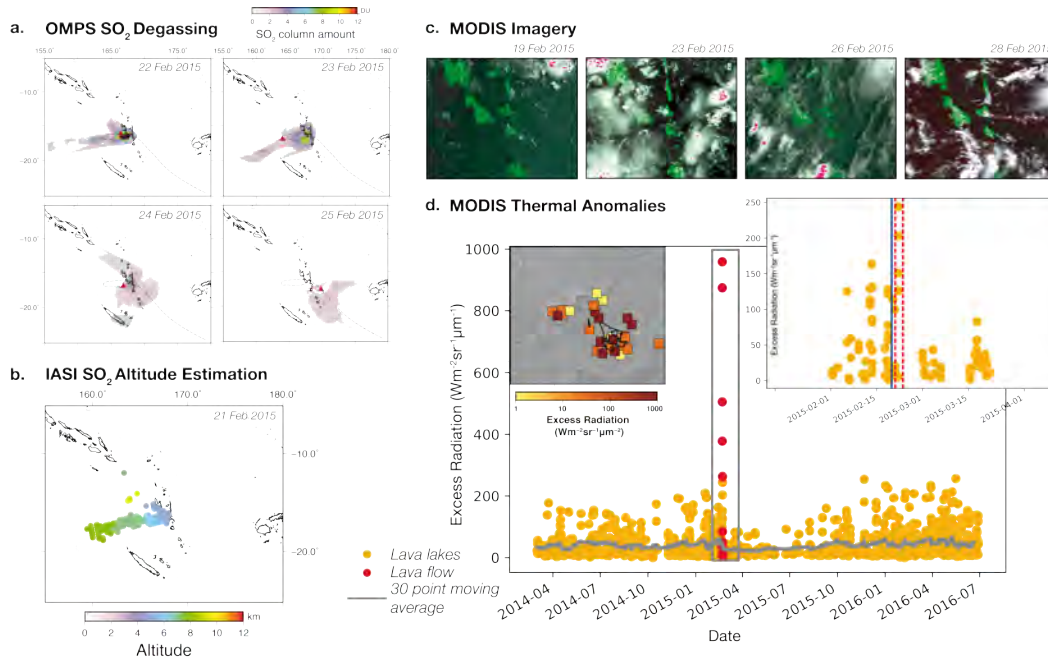| Dataset	Min/Max block size (m)	Deformation gradient threshold (m)	Maximum deformation threshold (m)
ALOS-2 ascending (2015/01/24–2015/03/21)	387/6190	0.05	0.13
ALOS-2 descending (2015/01/17–2015/03/14)	96/770	0.11	0.3

Figure S2. **a.** SO$_2$ column amount during the eruption measured by OMPS, using the TRM data product, as described in the Supporting Information Text S1. The largest plotted circles indicate pixels with SO$_2$ column amounts greater than 2 DU, while the smaller plotted circles indicate those above the 0.8–1 DU threshold. Datapoints with SO$_2$ column amounts higher than 12 DU are saturated with black. The dotted line is the trajectory calculated by HYSPLIT of SO$_2$ parcels emitted at 5 km altitude at 3h00 21 February 2015. The red triangle indicates the location of these SO$_2$ parcels at the time of the OMPS acquisition. **b.** The SO$_2$ altitude estimated by IASI at ∼10:30 UTC 21 February. **c.** MODIS images with the least cloud cover before, during, and after the eruption. The cloud cover extent may affect the detection of lava lake thermal anomalies during and after the eruption. **d.** A time series of excess radiation of thermal anomalies at Ambrym, as detected by MODIS. The orange dots correspond to lava lakes, while the red dots are due to lava effusion. The gray line is a moving average calculated using the lava lake thermal anomalies. The inset shows the lava lake thermal anomalies before, during, and after the eruption. The dark blue line indicates the timing of the 6.4 M$_w$ earthquake, and the dotted red lines indicate the maximum eruption duration. The inset in the top-left corner shows the thermal anomalies from 19–27 February in map view.
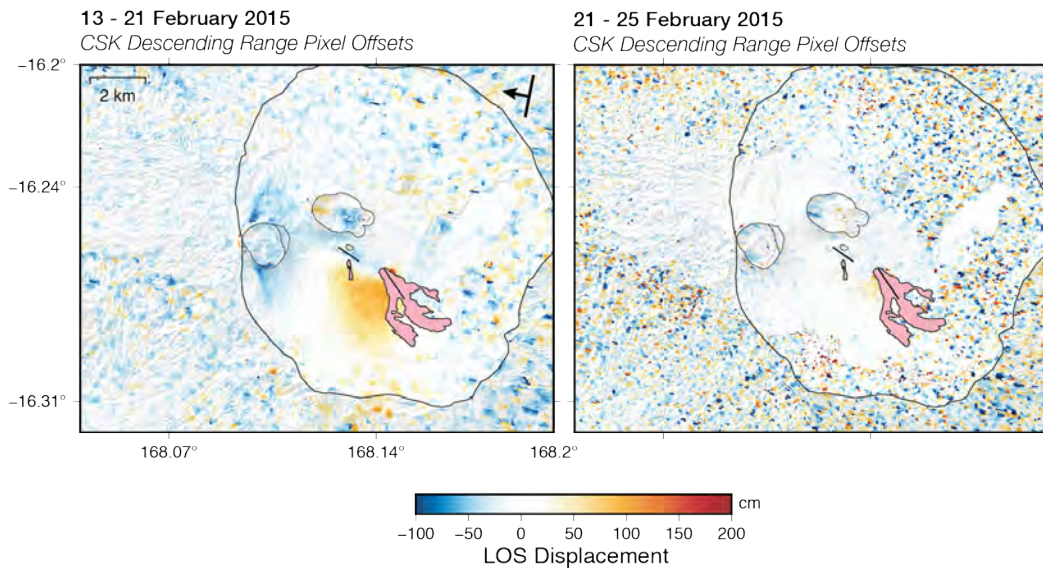
Figure S3.   LOS displacement field during the first and final 24 hours of the eruption, as measured by CSK range pixel offsets. Caldera ring-fault reactivation, and the majority of dike-induced deformation, occurred during the first 24 hours. All images were acquired at 6:00 UTC.
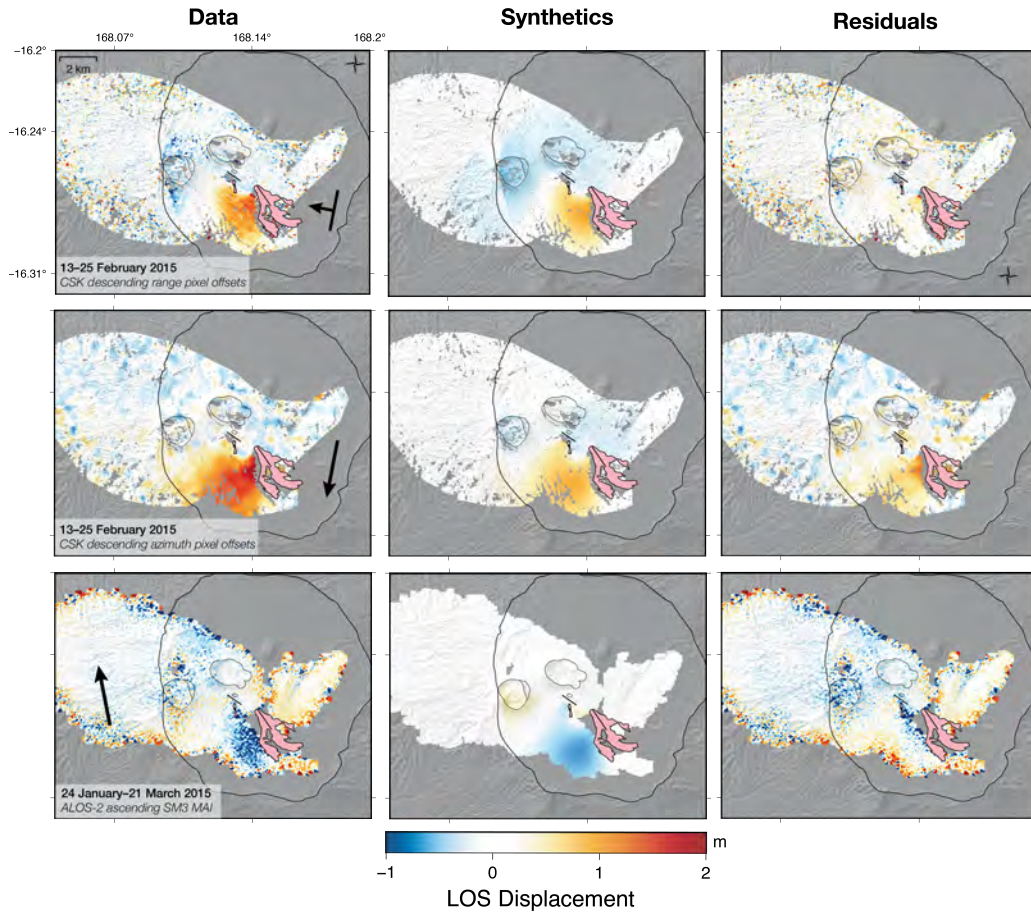
Figure S4. Data, synthetics, and residuals for datasets not included in the inversion. The left hand column shows the data, the middle column shows the ground displacements produced by the best-fit model from Inversion 3, projected into the LOS of each dataset. The right hand column shows the difference between the data and synthetic ground displacements. The colorbar is the same for all figures.
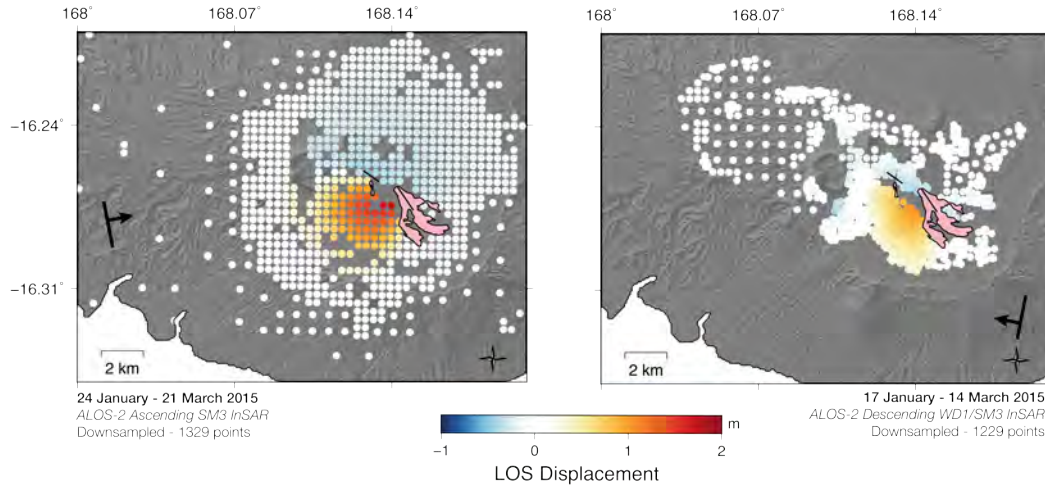
Figure S5. The ascending and descending interferograms, downsampled using the adaptive quadtree decomposition algorithm.
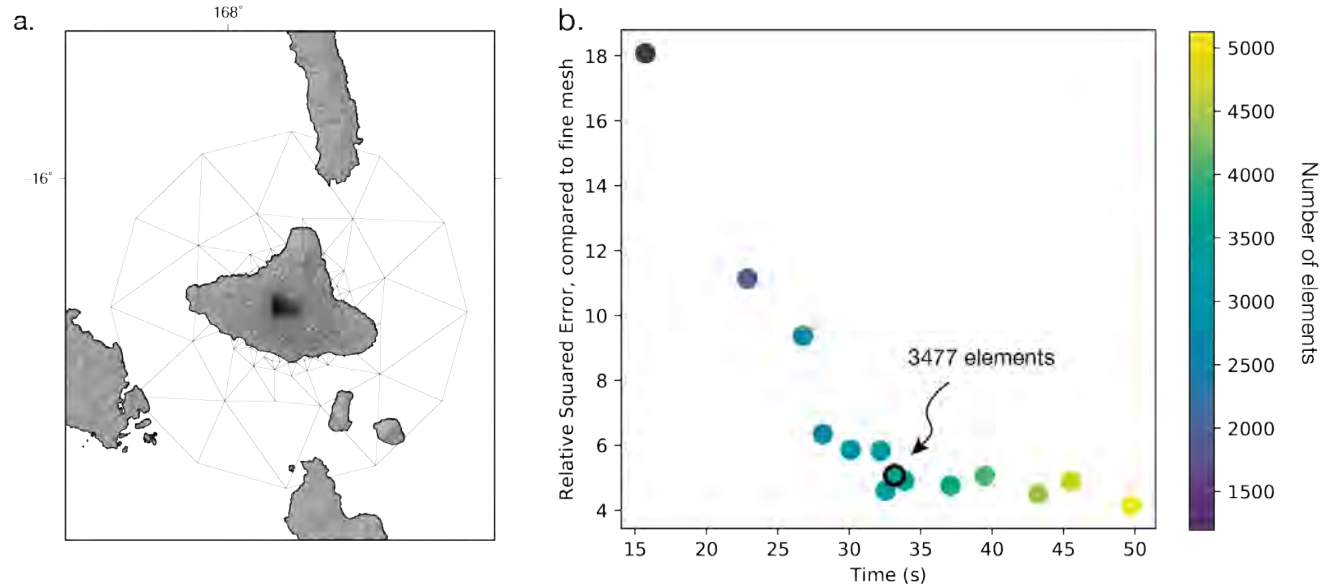

Figure S6. **a.** The topography mesh in map view. Elements are finer where the dike and fault intersect the surface. **b.** A plot showing the relative squared error of the calculated ground displacement using a particular topography mesh, compared to a very fine topography mesh (>25000 elements), versus run time of the forward model calculation. Color represents the number of elements in a particular mesh. The mesh used in the final inversions has 3477 elements, and is indicated by the dot outlined in black.
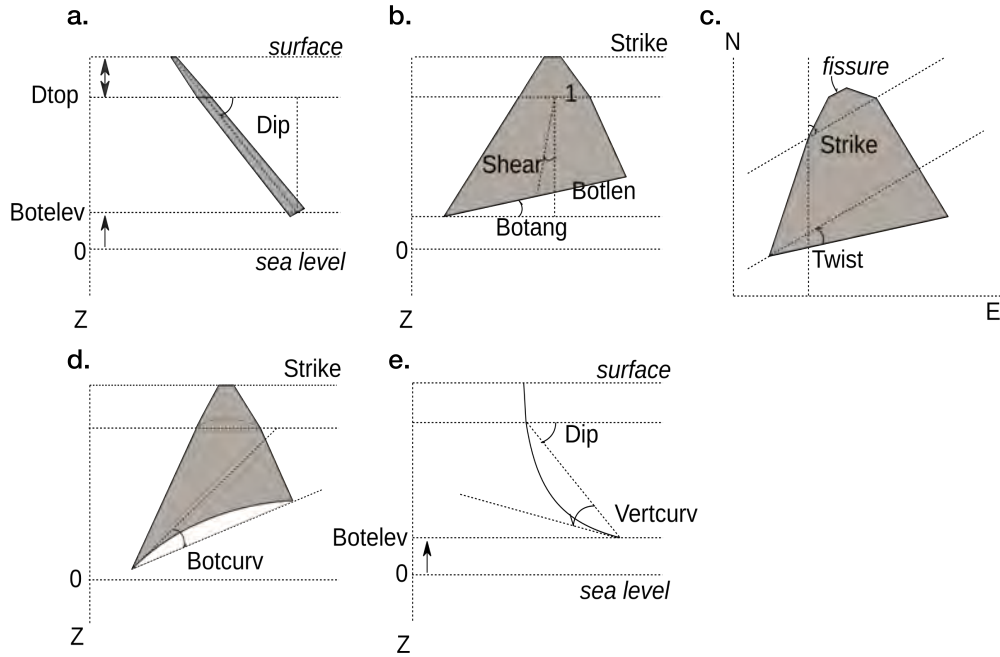
:

Figure S7. Non-linearly inverted dike geometry parameters. Figure from Smittarello et al. (2019). **a.** The *dip* is the angle measured from the surface, *dtop* is the distance measured from the surface echelons to the top of the quadrangle, and *botelev* is the distance measured from sea level to the quadrangle's bottom edge. **b.** The *shear* is the angle between the line perpendicular to the upper edge of the quadrangle's strike (clockwise angle from North), and the line formed by the center of the quadrangle's upper edge to the center of its bottom edge. The *botlen* is the ratio between the length of the quadrangle's upper and bottom edges. The *botang* is the angle of the bottom edge measured vertically from a line at the *botelv* elevation, parallel to the strike of the quadrangle's upper edge. **c.** The *twist* is the horizontal angle between the upper edge of the quadrangle's strike and the quadrangle's bottom edge. **d.** The *botcurv* is the angle between a line that connects both corners of the bottom edge and a line that is tangent to the bottom edge at one of the corners. **e.** The *vertcurv* is the vertical angle between a line connecting the center of the upper edge to the center of the bottom edge, and a line that is tangent to the center of the bottom edge.
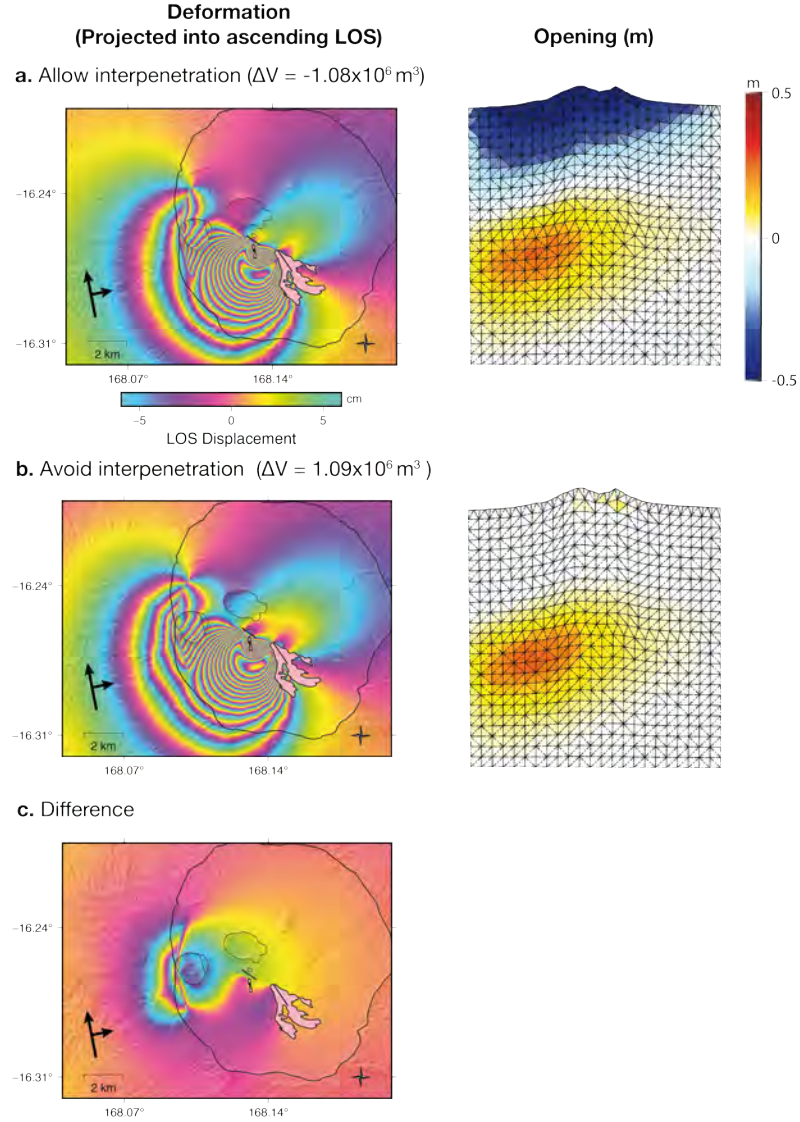
**Deformation
(Projected into ascending LOS)**

Opening (m)

a. Allow interpenetration (ΔV = -1.08x10^6 m^3)

b. Avoid interpenetration (ΔV = 1.09x10^6 m^3)

c. Difference

Figure S8. **a.** Using the best-fit model parameters found in Inversion 2 (see Table S5), we calculate a forward model allowing fracture wall interpenetration. The figure in the left hand column shows ground displacement resulting from both the fault slip and the dike opening, projected into the ascending line of sight. The figure in the right hand column shows the opening on the fault. **b.** The same as **a.**, but after applying a nonnegativity constraint (preventing interpenetration) in the forward model. **c.** The difference between the two displacement fields (∼20 cm).
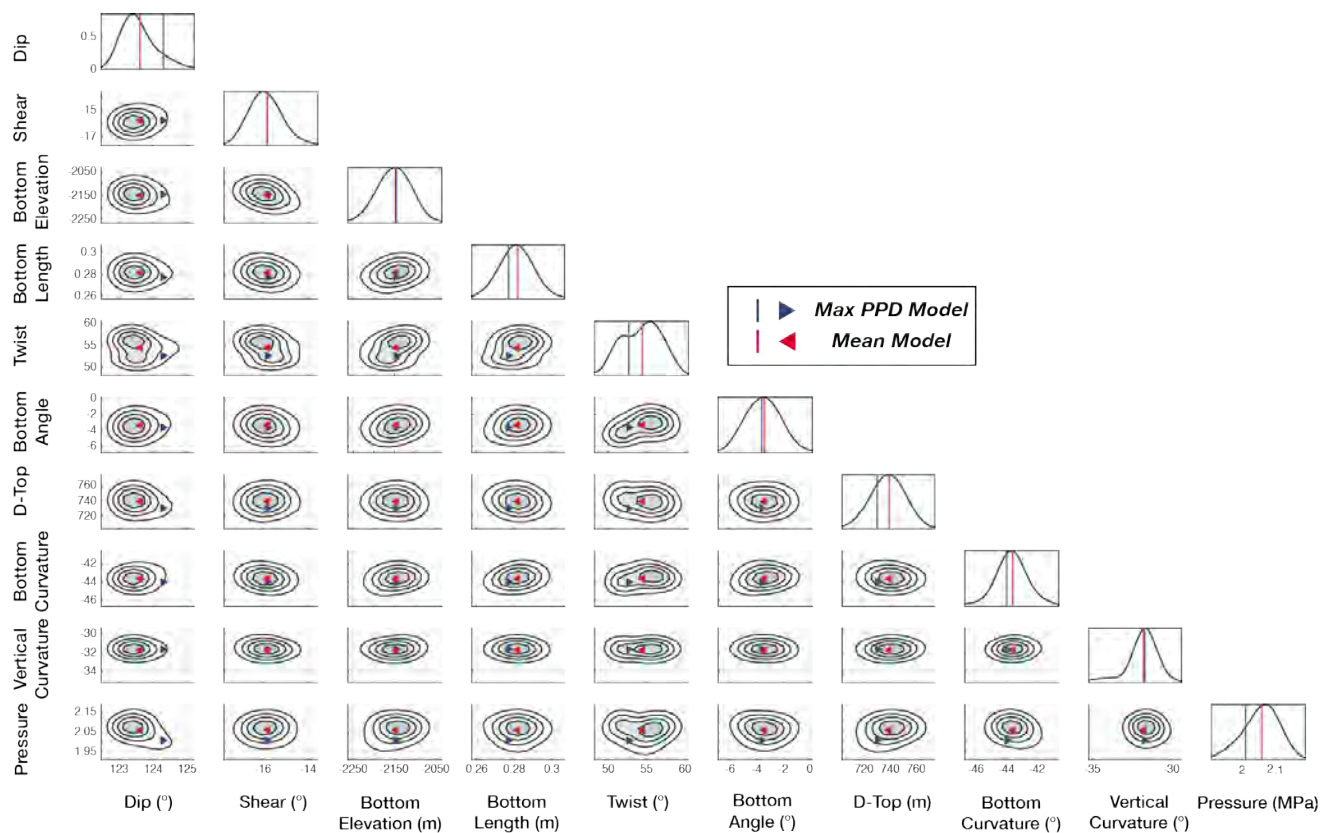
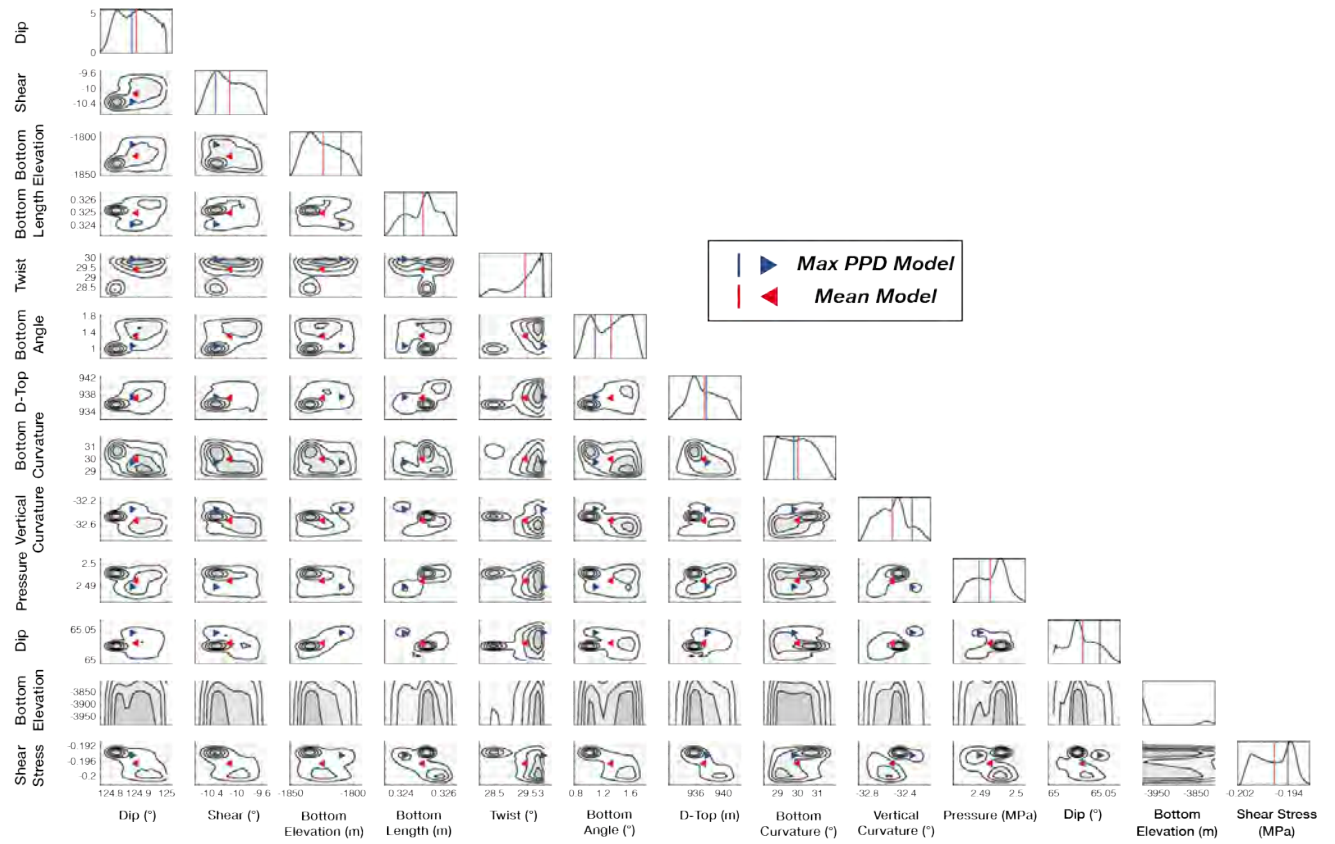**Figure S9.** Marginal posterior probability density functions for Inversion 1.

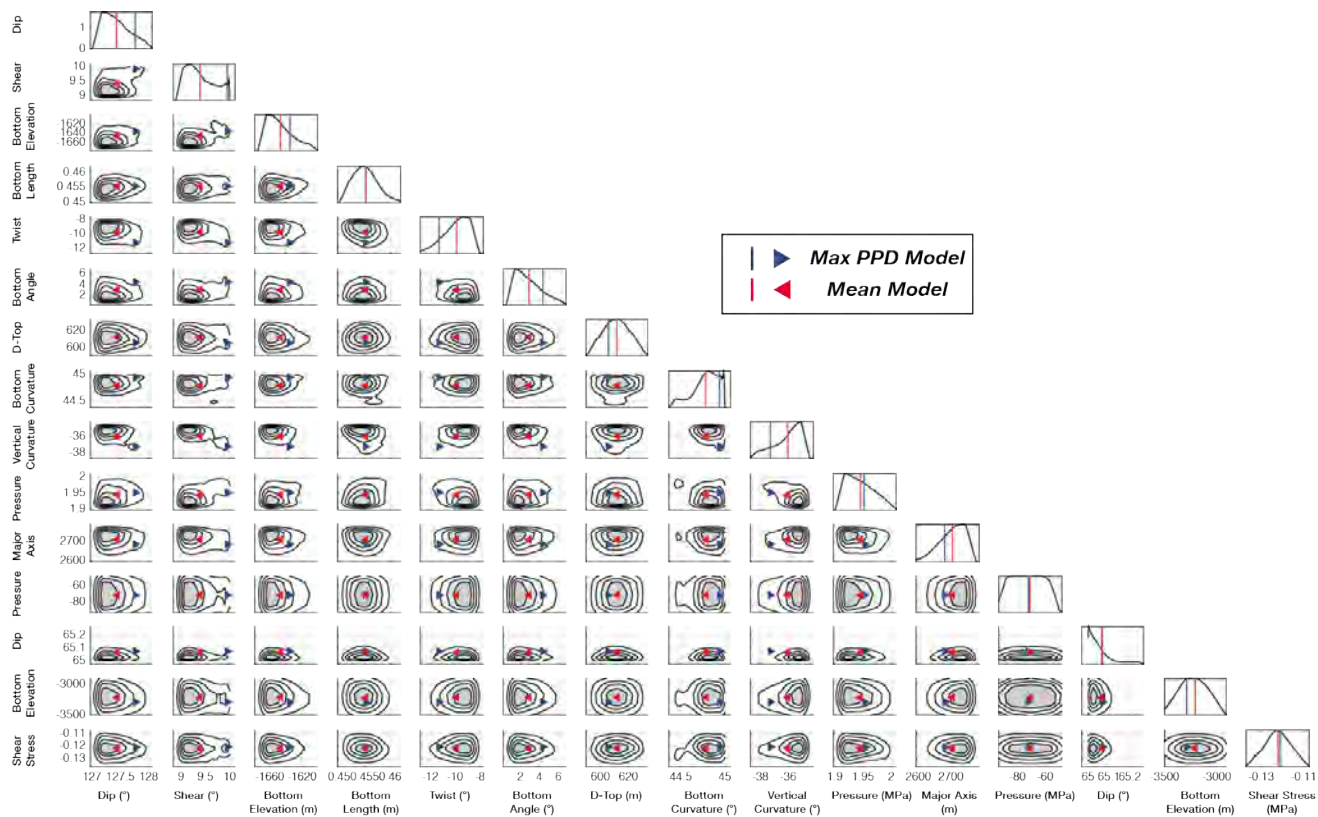**Figure S10.** Marginal posterior probability density functions for Inversion 2.

Figure S11. Marginal posterior probability density functions for Inversion 3.

Residuals

E-W displacements   N-S displacements   Vertical displacements

a.
c = 65 m
c/a = 0.05
V_{res} = 0.5 km³
ΔP/μ = 0.005

b.
c = 165 m
c/a = 0.12
V_{res} = 1.2 km³
ΔP/μ = 0.00375

c.
c = 335 m
c/a = 0.25
V_{res} = 2.4 km³
ΔP/μ = 0.00325

d.
c = 650 m
c/a = 0.5
V_{res} = 4.7 km³
ΔP/μ = 0.003

e.
c = 1000 m
c/a = 0.75
V_{res} = 7 km³
ΔP/μ = 0.0026

f.
c = 1300 m
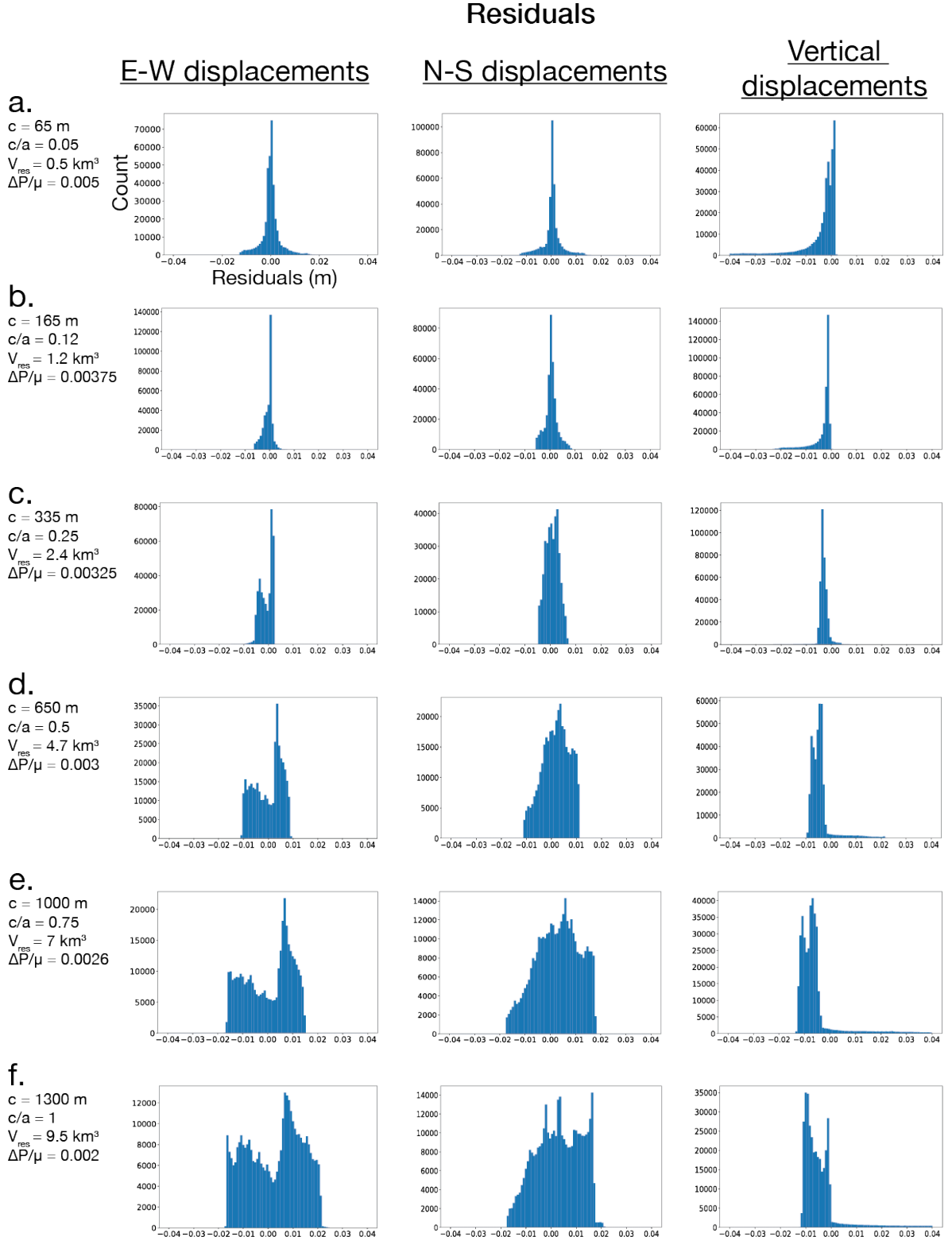c/a = 1
V_{res} = 9.5 km³
ΔP/μ = 0.002

Figure S12. Using the final source geometry estimated in Inversion 3, we increase the semi-minor axis c of the reservoir from 65 to 1300 m (increasing the aspect ratio $\frac{c}{a}$) in **a**–**f**. We run a forward model calculation, and subtract the displacement field from the displacement field calculated in Inversion 3. The histograms of the residuals are shown. An aspect ratio $\frac{c}{a} = 1$ indicates a spherical source (**f.**).
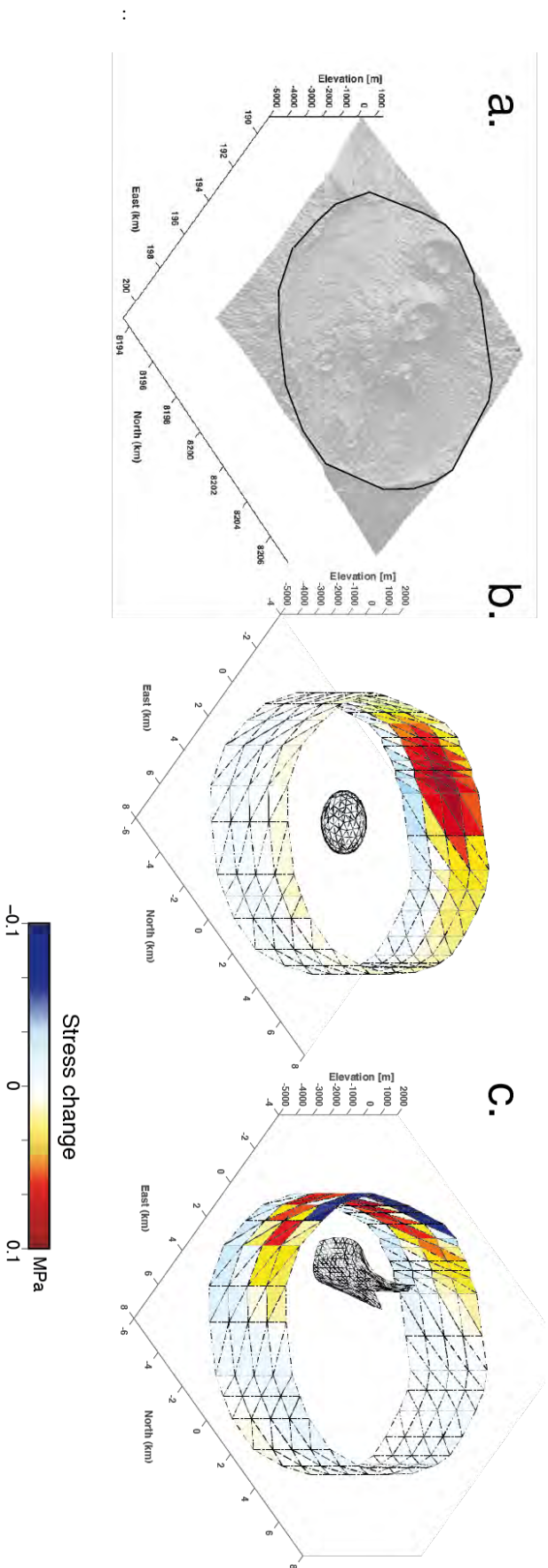
:

Figure S13. **a.** Oblique perspective of the topography mesh with a black line approximating the surface trace of the caldera ring-fault. **b.** Coulomb stress change on the ring-fault (assumed vertical, with a depth of 5 km) due to the depressurizing reservoir in Inversion 3. **c.** Coulomb stress change on the ring-fault due to the dike intrusion, whose geometry was estimated in Inversion 3.
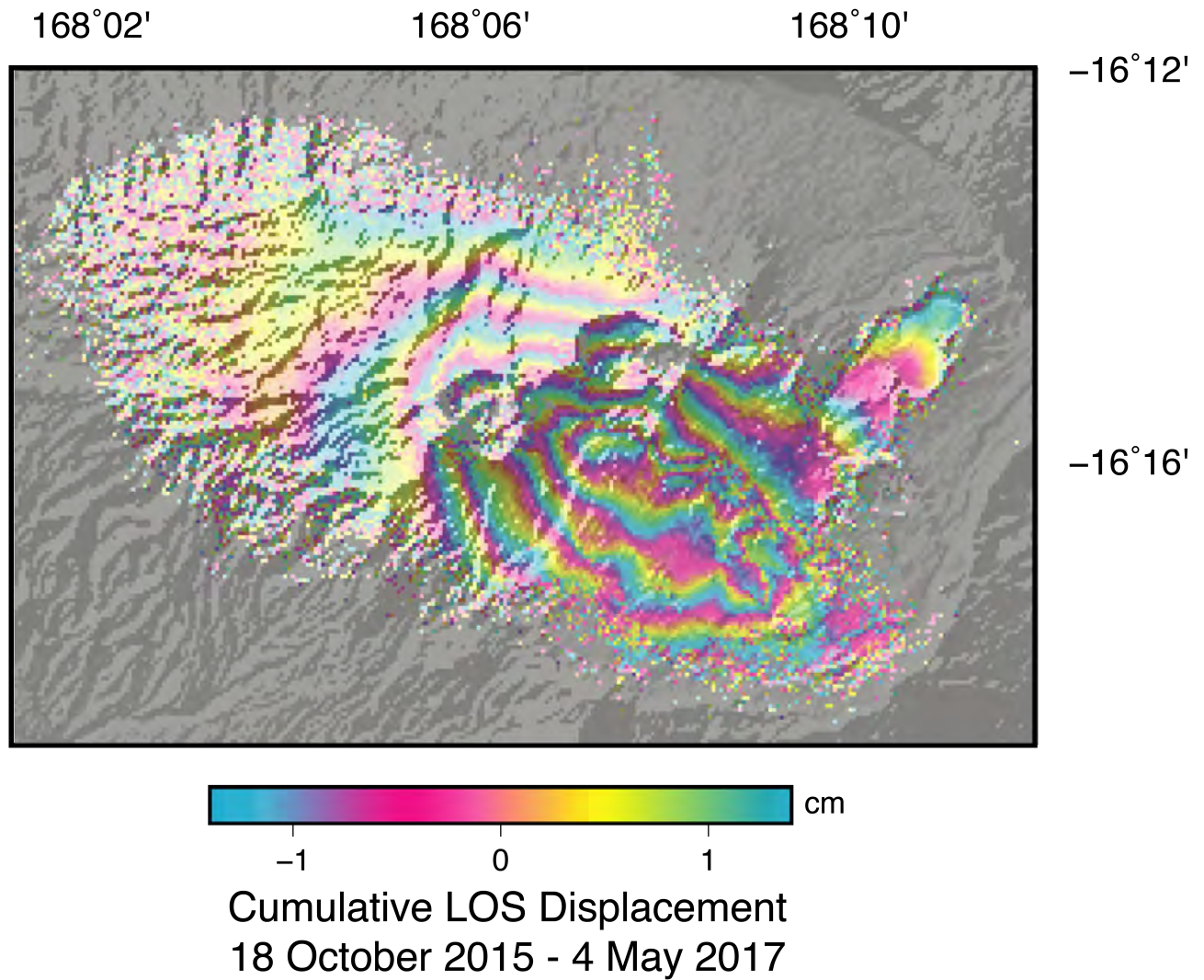
May 14, 2021, 2:05pm

Figure S14. Cumulative LOS lengthening (subsidence) measured by ESA's C-band SAR Satellite Sentinel-1 (ascending Track 81). A small baseline time series (Doin et al., 2011) was processed using interferograms spanning about two years after the 2015 eruption, from 18 October 2015 to 4 May 2017. Subsidence within the caldera dominated during this time period, at a rate of approximately 1 cm/month, elongated in the direction of the rift zone. Figure from Shreve et al. (2019).
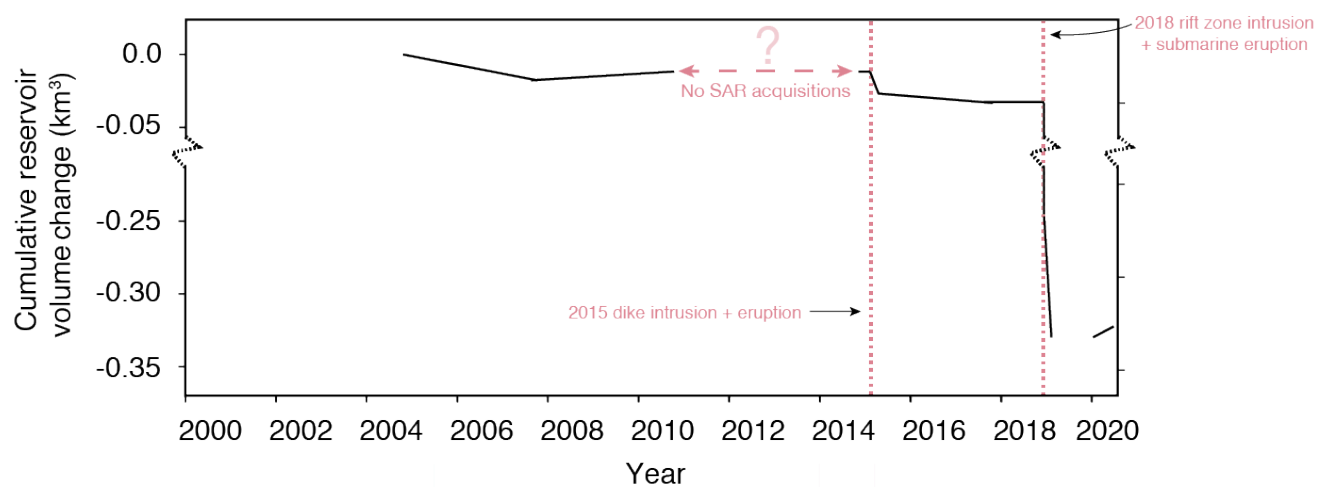
Figure S15. The cumulative reservoir volume change derived from geodetic models of InSAR measurements at Ambrym spanning 2004–2020. Eruptions are marked with red dotted lines. Figure from Shreve (2020).

Table S5. Mean and best-fit models from the non-linear inversion,

including 95% confidence intervals and the full explored parameter bounds.

Inversion	Parameter	Mean ± Standard Deviation	Best Fit Model	95% Confidence Interval	Explored Interval
Inversion 1					
Dike	Dip (°)	123.61 ± 0.51	124.30	[122.79, 124.89]	[0, 180]
	Shear (°)	-15.805 ± 0.733	-15.804	[-17.243,-14.042]	[-80,80]
	Bottom Elevation (m)	-2146.8 ± 42.2	-2144.4	[-2236.9,-2059.7]	[-8000, -500]
	Bottom Length	0.2818 ± 0.0093	0.2780	[0.2629,0.3011]	[0.2,10]
	Twist (°)	54.419 ± 2.545	52.658	[49.587,59.030]	[-70,70]
	Botang (°)	-3.4197 ± 1.3534	-3.6056	[-6.086,-0.6328]	[-45,45]
	D-Top (°)	739.33 ± 12.93	730.07	[711.18,766.30]	[0,3000]
	Bottom Curvature (°)	-43.587 ± 1.08	-43.979	[-46.021, -41.278]	[-60,60]
	Vertical Curvature (°)	-31.772 ± 1.01	-31.680	[-34.571,-30.036]	[-60,60]
	Pressure (MPa)	2.2807 ± 0.0545	2.2269	[2.1501,2.3884]	[1,10]
Inversion 2					
Dike	Dip (°)	124.89 ± 0.06	124.88	[124.79, 124.99]	[110,125]
	Shear (°)	-10.115 ± 0.254	-10.336	[-10.536,-9.649]	[-30,10]
	Bottom Elevation (m)	-1823.7 ± 12.8	-1809.6	[-1843.9,-1799.4]	[-3000,-1000]
	Bottom Length	0.3250 ± 0.0007	0.3241	[0.3236,0.3262]	[0,0.5]
	Twist (°)	29.433 ± 0.502	29.959	[28.293,29.977]	[-30,30]
	Botang (°)	1.3168 ± 0.2506	1.0801	[0.8937,1.7110]	[-20,20]
	D-Top (°)	937.23 ± 2.17	937.54	[933.30,941.34]	[800,1500]
	Bottom Curvature (°)	30.015 ± 0.786	29.812	[28.292,29.976]	[-45,45]
	Vertical Curvature (°)	-32.533 ± 0.156	-32.326	[-32.805,-32.216]	[-60,60]
	Pressure (MPa)	2.723 ± 0.0125	2.7195	[2.7141,2.7312]	[1,6]
Fault	Dip (°)	65.029 ± 0.015	65.046	[65.003,65.058]	[65,90]
	Shear (°)	0	-	-	[0,0]
	Bottom Elevation (°)	-3993.7 ± 6.0	-3990.4	[-3964.6,-3823.2]	[-4000,-500]
	Bottom Length	1	-	-	[1,1]
	Twist (°)	0	-	-	[0,0]
	Botang (°)	0	-	-	[0,0]
	D-Top (°)	0	-	-	[0,0]
	Bottom Curvature (°)	0	-	-	[0,0]
	Vertical Curvature (°)	0	-	-	[0,0]
	Shear Stress (MPa)	-0.2145 ± 0.0027	-0.2121	[-0.2196,-0.2097]	[-1.5,0]
Inversion 3					
Dike	Dip (°)	127.44 ± 0.23	127.77	[127.09,127.94]	[110,140]
	Shear (°)	9.3932 ± 0.2879	9.9471	[8.9810,9.9608]	[-30,10]
	Bottom Elevation (m)	-1646.5 ± 16.2	-1634.8	[-1669.6,-1609.5]	[-3000,-1000]
	Bottom Length	0.4552 ± 0.00239	0.4552	[0.4511,0.4606]	[0,0.5]
	Twist (°)	-9.867 ± 1.026	-11.280	[-12.210,-8.300]	[-70,70]
	Botang (°)	2.9067 ± 1.3832	4.3797	[0.9362,6.0635]	[-50,50]
	D-Top (°)	611.83 ± 9.06	605.76	[594.75,628.76]	[300,1500]
	Bottom Curvature (°)	44.783 ± 0.147	44.939	[44.443,44.985]	[-45,45]
	Vertical Curvature (°)	-36.016 ± 0.989	-37.271	[-38.198,-34.694]	[-60,60]
	Pressure (MPa)	2.1177 ± 0.0244	2.1245	[2.0786,2.1726]	[1,5]
Fault	Dip (°)	65.065 ± 0.063	65.07	[65.003,65.232]	[65,90]
	Shear (°)	0	-	-	[0,0]
	Bottom Elevation (°)	-3207.4± 73.8	-3288.8	[-3434.3,-2974.7]	[-4000,-500]
	Bottom Length	1	-	-	[1,1]
	Twist (°)	0	-	-	[0,0]
	Botang (°)	0	-	-	[0,0]
	D-Top (°)	0	-	-	[0,0]
	Bottom Curvature (°)	0	-	-	[0,0]
	Vertical Curvature (°)	0	-	-	[0,0]
	Shear Stress (MPa)	-0.13271 ± 0.00594	-0.13167	[-0.1454,-0.12052]	[-1.5,0]
Reservoir	X0 (UTM)	193142	-	-	[193142,193142]
	Y0 (UTM)	8201632	-	-	[8201632,8201632]
	Semi-major Axis (m)	2704.8 ±40.1	2681.4	[2615.0,2764.4]	[1000,6000]
	Semi-minor Axis (m)	5	-	-	[5,5]
	Depth (m)	-4100	-	-	[-4100,-4100]
	Strike (°)	0	-	-	[0,0]
	Dip (°)	0	-	-	[0,0]
	Plunge (°)	0	-	-	[0,0]
	Pressure (MPa)	-77.335 ± 2.770	-78.445	[-96.184,-57.711]	[-350,0]

:

Table S6. Volume, opening, and slip estimates for all inversions. Final estimates have been scaled by the value in the last column, as described in the text.

Inversion	Dike					Fault		Reservoir			
	ΔV (m³)	Opening$_{avg}$ (m)	Opening$_{max}$ (m)	Slip$_{avg}$ (m)	Slip$_{max}$ (m)	Slip$_{avg}$ (m)	Slip$_{max}$ (m)	ΔV (m³)	Opening$_{avg}$ (m)	Opening$_{max}$ (m)	Scalar
Inversion 1	2.39×10^{7}	1.78	2.61	0.43	1.18		-	-	-	-	1.108
Inversion 2	2.30×10^{7}	1.98	2.97	0.37	1.00	0.39	1.02	-	-	-	1.092
Inversion 3	2.38×10^{7}	1.73	2.74	0.43	1.14	0.44	0.91	-1.45×10^{7}	-0.90	-2.91	1.088